

The symmetric dust shell and the central star of the bipolar planetary nebula NGC 6537 ^{*} †

M. Matsuura¹, A.A. Zijlstra¹, M.D. Gray¹, F.J. Molster², L.B.F.M. Waters^{3,4}

¹*School of Physics and Astronomy, University of Manchester, Sackville Street, P.O. Box 88, Manchester M60 1QD, UK*

²*ESTEC, European Space Agency, Keplerlaan 1, 2201 AZ Noordwijk, The Netherlands*

³*Astronomical Institute ‘Anton Pannekoek’, University of Amsterdam, Kruislaan 403, 1098 SJ, Amsterdam, The Netherlands*

⁴*Instituut voor Sterrenkunde, Katholieke Universiteit Leuven, Celestijnenlaan 200B, 3001 Heverlee, Belgium*

Accepted. Received; in original form

ABSTRACT

We present high-resolution images of the strongly bipolar planetary nebula NGC 6537, obtained with HUBBLE SPACE TELESCOPE and with the infrared adaptive optics system on the VERY LARGE TELESCOPE. The central star is detected for the first time. Using the multi-band photometry and constraints from the dynamical age of the nebula, we derive a temperature in the range $1.5\text{--}2.5 \times 10^5$ K, a luminosity $\sim 10^3 L_{\odot}$, and a core mass $M_c \approx 0.7\text{--}0.9 M_{\odot}$. The progenitor mass is probably in the range $M_i = 3\text{--}7 M_{\odot}$. The extinction map shows a largely symmetric, and compact dust structure, which is most likely a shell, located at the neck of the bipolar flow, only 2–4 arcsec from the star. The dust shell traces a short-lived phase of very high mass loss at the end of the AGB. The dynamical age of the shell and bipolar lobes are very similar but the morphologies are very different. The data suggests that the mass loss during the ejection of the compact shell was largely spherically symmetric, and the pronounced bipolarity formed afterwards. The dynamical ages of the bipolar lobes and dust shell are similar, which is consistent with suggestions that bipolar structures form in a run-away event at the very last stages of the AGB mass loss. The inner edge of the dust shell is ionized, and PAH emission is seen just outside the ionized gas. We associate the PAH emission with the photo-dissociation region of the molecular shell.

Key words: (ISM:)Planetary nebulae:individual:NGC 6537 – (ISM:)dust, extinction – stars: evolution

1 INTRODUCTION

At the end of the asymptotic giant branch (AGB) phase, stars experience high mass loss rates ($10^{-7}\text{--}10^{-6} M_{\odot} \text{ yr}^{-1}$), which may increase by a further order of magnitude during helium shell flashes (Habing 1996). The high mass loss terminates once the hydrogen envelope of the star is almost fully removed. During the subsequent post-AGB phase, the temperature of the central star increases, and eventually the surrounding ejected material is ionised, and detected as a planetary nebula (PN).

During the so-called superwind, the objects suffer high self-extinction from dust which forms in the ejecta; the absorbed radiation is re-emitted at infrared wavelengths. The IRAS photometric observations show that the infrared colour temperature decreases from 1000 K in AGB stars to a few hundred Kelvin in post-AGB stars and PNe (van der Veen and Habing 1988; Zijlstra et al. 2001): as the star evolves, the circumstellar shell expands and the temperature of the circumstellar shell decreases.

Planetary nebulae commonly show non-spherically symmetric morphologies, often elliptical or bipolar. These may trace the interaction of a fast wind ($> 1000 \text{ km s}^{-1}$) from the central star of the PN, with the slow wind ($20\text{--}30 \text{ km s}^{-1}$) dating from the AGB (Kwok 1982). The expansion velocity of the AGB shell is $20\text{--}30 \text{ km s}^{-1}$ while the fast wind from the PN is more than 1000 km s^{-1} . This interaction of the winds can enhance shapes which are already present in the original AGB wind. However, it is still not clear how the original shape is created. There is evidence that bipolar

^{*} Based on observations with European Southern Observatory, Very Large Telescope with an instrument, ISAAC and NAOS-CONICA (the proposal numbers: 65.D-0395A, 72.D-0766A).

† Based on observations made with the NASA/ESA Hubble Space Telescope, obtained from the ESA/ECF Data Archive. HST is operated by the Association of Universities for Research in Astronomy, Inc., under NASA contract NASA 5-26555. These observations are associated with program no. 8345.

PNe tend to have higher mass progenitors (Kastner et al. 1996), from helium and nitrogen enrichments characteristic of type I PN (Peimbert 1978). These have likely progenitor masses of $> 2.5 M_{\odot}$. Magnetic fields have been suggested, or a binary companion may give rise to a circumbinary dusty disk (Balick and Frank 2002). A warped disk has been suggested to give rise to multipolar PNe (Icke 2003). Some AGB stars show a cold detached dust shell. Infrared images have resolved some of these shells, which appear not to show deviations from symmetry (Izumiura et al. 1996; Olofsson et al. 2000).

Here, we report high spatial resolution images of the PN NGC 6537, which shows one of the most pronounced bipolar outflows seen among PNe. It is a type-I PN, which is overabundant nitrogen and helium (c.f. Pottasch et al. 2000b). The central star of NGC 6537 has not previously been detected (Pottasch 2000a). We use HST images to create an extinction map: this traces the dust at far higher resolution than can be achieved using far-infrared dust emission. We find that the extinction inside this nebula is not uniform, but is concentrated in a compact dust shell. The central star is detected for the first time, only 0.5 arcsec away from the brightest part of the nebula. Using the photometry in the optical HST images and the infrared adaptive optics image, the luminosity of the central star is constrained.

2 OBSERVATIONS

We observed NGC 6537 with the Adaptive Optics (AO) system, NAOS, and the infrared camera CONICA, on the Very Large Telescope (VLT) on the 6th of March 2004 (in UT). The exposure time was 28 minutes. We used the S27 camera with a pixel scale of 27 milliarcsec. The Ks-band filter was used. The dichroic for AO was VIS, i.e., the visual camera was used. The AO reference star was S 300100217909 ($V=14.8$ mag) from the Guide Star Catalogue, which is approximately 22 arcsec away from NGC 6537's central star. The approximate spatial resolution of the final image is 0.22 arcsec (RA orientation) and 0.16 arcsec (Dec orientation), estimated from nearby stars; but the spatial resolution varies slightly even within the image. The weather was clear. The internal calibration lamp was used for flat fielding. The jittering technique was used to minimize the effect of hot pixels. The sky background was estimated from a medium of jittered frames with slightly different positions.

NGC 6537 was observed with the Hubble Space Telescope (HST) in the programme 6502 (P.I. B. Balick). In total, HST images were obtained with 8 different filters (Table 1). We retrieved the images from data archives at the Space Telescope - European Coordinating Facility (ST-ECF). The data were taken on the 12th of September 1997 with the Wide Field Planetary Camera 2 (WFPC2), which has four 800×800 pixel detectors. The main region of interest for this paper, close to the centre, is covered with the Wide Field Cameras which have a 0.1 arcsec pixel scale. The spatial resolution is limited by the pixel scale, as the point-spread function is under-sampled, but slightly better than that because multiple images were taken for a single band (with the exception of F487N and F547M). We use the pipeline-reduced data. The PHOTFLAM parameter is used for the flux calibration. Spike noise due to cosmic rays

Table 1. The log of HST observations.

Filter	Wave [Å]	BW [Å]	CS	T_{ex}	Lines
F673N	6732	30	yes	400sec \times 1,500sec \times 1	[SII]
F631N	6306	13	yes	400sec \times 3	[OI]
F658N	6591	30	no	400sec \times 3	[NII]
F656N	6564	54	no	400sec \times 3,40sec \times 1	H α
F547M	5483	205	yes	40sec	
F502N	5013	48	no	300sec \times 2, 400sec \times 1	[OIII]
F487N	4865	32	no	500sec	H β
F469N	4695	17	no	400sec	[HeII]

Wave: wavelength

BW: band width (for photometric calibration; not equivalent with FWHM)

CS: detection of the central star

T_{ex} : exposure time per frame (some bands have multiple exposures)

Line: major lines inside the filter

was removed using the exposures with slightly different positions if multiple images were obtained within the same filter, exceptions being F487N and F547M which have a single exposure for each. For F487N, we removed the cosmic ray noise by taking the medium over nearby regions.

Our PAH image was obtained with ISAAC on the VLT. The data were acquired on 13th of August, 2000 in service mode. We used the *eclipse* and IDL packages for data reduction. Images were obtained with two filters: NB_3.28 (PAH band) and NB_3.21 (continuum). Total exposure time was 7 min for each band. Optical seeing was 0.56–0.83 and 0.47–0.66 and the measured infrared seeing was 0.53–0.61 and 0.47–0.54 arcsec (FWHM), respectively, which was measured from the nearby stars. After the flux calibration with reference to a standard star HR 7446, the continuum was subtracted, and a PAH image was created.

3 RESULTS : THE CENTRAL REGION OF NGC 6537

The entire field at H α is shown in Fig. 1. It shows an extended bipolar outflow, and a dense core with a size of $\sim 5 \times 5$ arcsec² at the centre. The bipolar lobes have the appearance of an hourglass, seen close to edge-on; the north-western lobe is slightly fainter and may be pointing away from us. At the faintest levels, the nebula extends beyond the WFPC2 field of view. The lobes extend over 1 arcminute, and are oriented roughly NE-SW. The core consists of bright arcs tracing a shell surrounding an irregular cavity (Fig. 2). The cavity is between 2.5 and 4 arcsec in diameter, with the long axis roughly (but not perfectly) aligned with the bipolar flow. The arcs have thickness of approximately 1 arcsec. There is a much fainter extended shell with a diameter of 6×2.5 arcsec, with the major axis oriented EW. Apart from the cavity elongation, none of the structures shows an obvious alignment with the bipolar axis.

The Ks-band image is shown in Fig. 3. Several arcs are detected, which are the same as those found in the central region of the H α image, as discussed later. The dominant source of emission in the Ks-band is likely to be free-free and

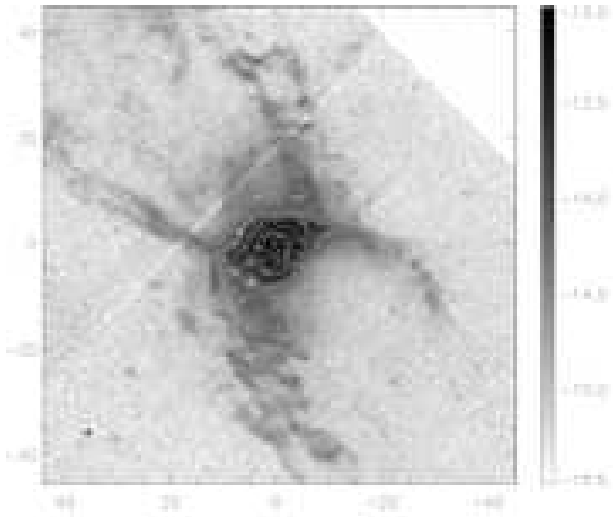


Figure 1. The entire field of the planetary nebula NGC6537 in $H\alpha$. North is top and east is left. The x-axis is the RA offset in arcsec and y-axis is the Dec offset in arcsec, for all of the images in this paper. The unit is $\text{erg cm}^{-2}\text{s}^{-1}\text{arcsec}^{-2}$, contours show $\log(I_\nu) = -14, -13.6, -13.3, -13, -12.6, -12.3, -12$.

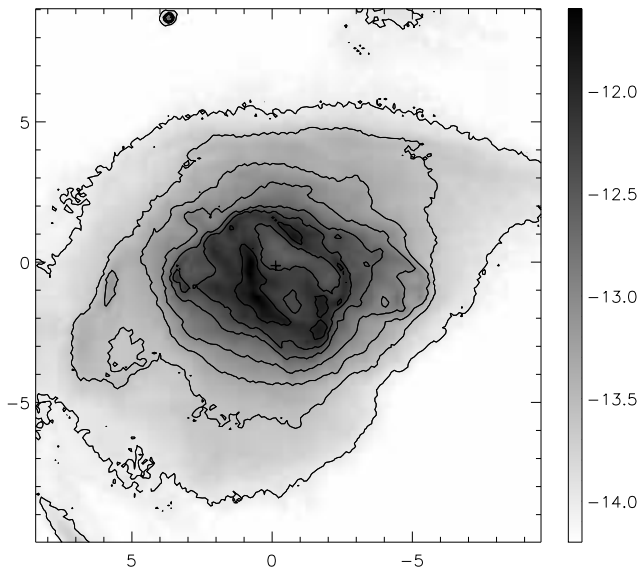


Figure 2. The central region of $H\alpha$ (I_ν) image in the unit of $\text{erg cm}^{-2}\text{s}^{-1}\text{arcsec}^{-2}$, contours show $\log(I_\nu) = -14, -13.6, -13.3, -13, -12.6, -12.3, -12$. (same as Fig. 1)

bound-free continuum emission from the ionized gas. Only regions of higher emission measure in the ionised region are detected at the Ks-band. The much fainter bipolar wings are not detected.

Table 2. Measured fluxes of the central star. The error includes only the measurement error of aperture photometry. Systematic errors, such as contribution of nebula into the aperture or the error of calibration star (for Ks band) are not included.

Filter	Wavelength [\AA]	Magnitude	Flux [Jy]
F673N	6732	21.74 ± 0.54	$[11.0 \pm 7.2] \times 10^{-6}$
F631N	6306	21.34 ± 0.33	$[14.2 \pm 5.1] \times 10^{-6}$
F547M	5483	21.56 ± 0.22	$[8.6 \pm 2.0] \times 10^{-6}$
Ks	2.18×10^4	18.63 ± 0.61	26×10^{-6}

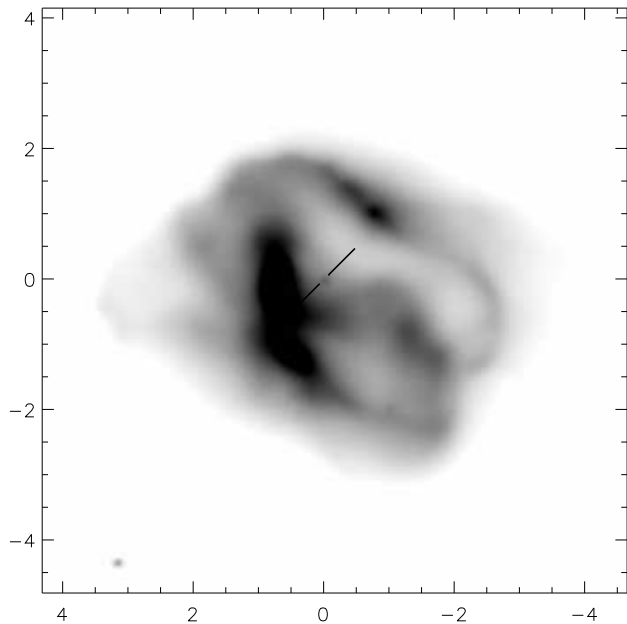


Figure 3. Ks-band image (in linear scale). The lines show the position of the central star.

3.1 Detection of the central star

The star is clearly detected, separated from the extended nebula in the high spatial resolution images with HST and NACO. The coordinates of the newly discovered central star are $\text{RA} = 18^{\text{h}}05^{\text{m}}13^{\text{s}}.03$, $\text{Dec} = -19^{\circ}50'34''.4$ (J2000).

The Ks magnitude of the central star is 18.6 ± 0.6 mag, which is derived from aperture photometry with a radius of 5 pixels. The magnitude is referenced to nearby stars in the same frame: 2MASS 18051346–1950277 (Ks= 13.382 ± 0.166 mag) and 2MASS 18051378–1950407 (Ks= 12.674 ± 0.040 mag). The uncertainty of 0.61 mag is the measurement error only: the uncertainty from the magnitude calibration is not included. There might be some flux contribution from the nebula within the aperture, which may not have been removed completely. The background level (including the contribution of nebula) is estimated from circular with inner radius of 150 % and outer radius of 200 % of the aperture size.

The central star is also detected in three HST filters, two of which are shown in Figs. 4 and 5. The results of aperture photometry with a radius of 2 pixel are listed in Table 2. The largest uncertainty of the magnitudes is due to the contribution of nebula and the flux missed outside of

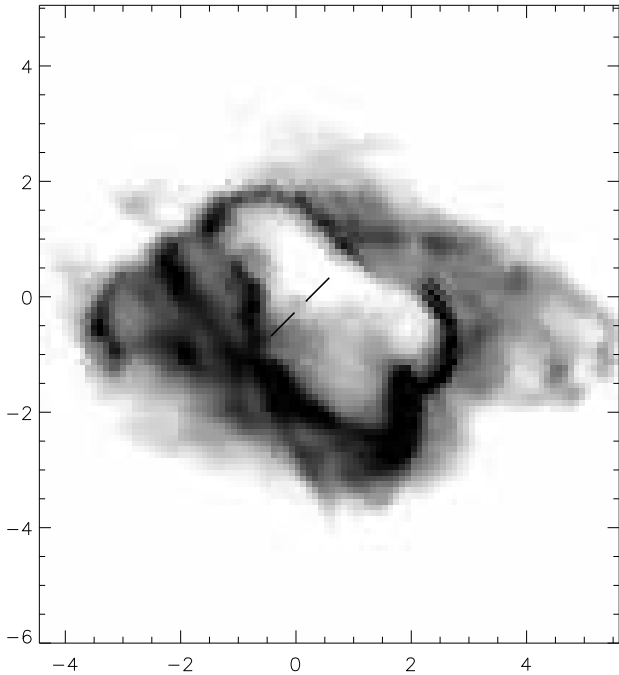


Figure 4. HST F673 band image (in logarithmic scale). The lines show the position of the central star.

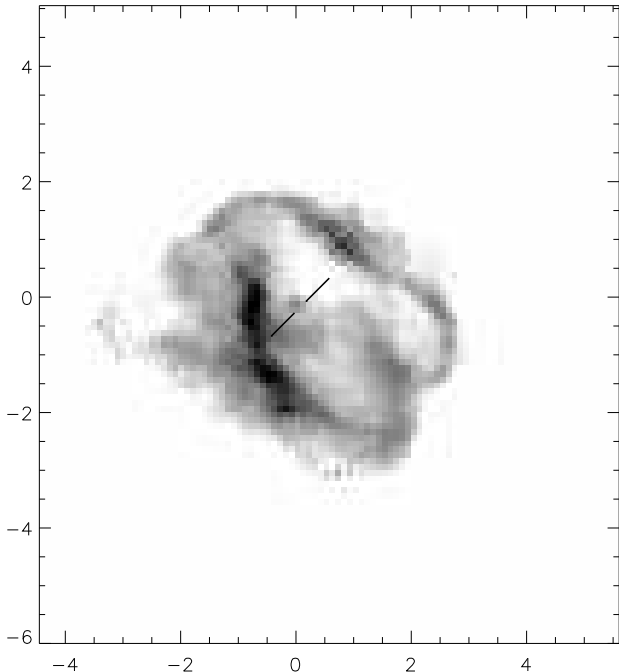


Figure 5. HST F547M band image (in logarithmic scale). The lines show the position of the central star.

the radius. These systematic errors are not counted in these errors. F547M is the only medium-band filter and this filter is sensitive to continuum. In addition, the central star is detected in two narrow band filters. The remaining five filters which were used for the observations did not give detections. The star is too faint to be detected in the narrow blue filters (F487N, F469N and F502N; Fig. 6), due to extinction, while the F656N and F658N filters contain strong ionised lines within the filter transmission ($H\alpha$ and $[NII]$), and the contamination of these ionized lines from the nebula prevents detection of the star (Fig. 2). All three HST filters where the central star was detected have only weak atomic lines within their wavelength coverage.

Pottasch (2000a) reported a non-detection of the central star, using the same HST data. The under-sampling of the Wide Field Camera can make it difficult to distinguish a faint star from spike noises due to the cosmic ray hits, and this may be the reason for their non-detection. However, comparison with the well-sampled Ks-band images confirms the central star detection in three images.

Kaler and Jacoby (1989) predicted that the central star of NGC 6537 should be about $V = 19.67$ mag, and Pottasch (2000a) estimate $V = 22.4$ mag. We obtained magnitudes in a ‘continuum band’ at 5483 \AA , which is very close to the V-band. Assuming that the visual magnitude is the same as that in the F547M band, 21.6 ± 0.22 mag and ignoring the systematic errors, our measured magnitude is just between the predicted values of Pottasch (2000a) and Kaler and Jacoby (1989).

A detection of the central star has been suggested by Reay et al. (1984), as a ‘stellar-like condensation to the east of centre.’ However, Gathier and Pottasch (1988) and Pottasch (2000a) show that this detection is not a star but a condensation in the nebula. We agree with the latter view, since the nearby condensed part of nebula is only ~ 0.7 arcsec away from the star, and could not have been resolved from the star at 2 arcsec seeing (Reay et al. 1984).

3.2 The extinction map

The extinction map is estimated from HST $H\alpha$ (F656N) and $H\beta$ (F487N) images. We assume an electron temperature of 15 000 K, and an electron density of $1 \times 10^4 \text{ cm}^{-3}$ (Pottasch et al. 2000b). The $H\alpha$ and $H\beta$ intensity ratio of 2.79 (Case B) is used (Storey and Hummer 1995). The sensitivity is limited by $H\beta$ data (Fig. 6). The image is smoothed to 0.2 arcsec pixel scale. This also removes any difference in resolution between $H\alpha$ and $H\beta$.

Fig. 7 shows the extinction map of the core region of NGC 6537. The extinction within the core is non-uniform, showing the presence of internal extinction within the PN. At the centre, the extinction $E(H\beta - H\alpha)$ is 1.4–1.5 mag, while it increases up to 2.2 mag at 4 arcsec away. The thickness of the high extinction region is about 2 arcsec. This high extinction shell shows the presence of a detached dust shell, located far inside the extended planetary nebula. The inner cavity of the dust shell shows an elongation along the bipolar outflow which is towards the north-east(=left-top in the figure), and the south-west(=right-bottom). The central star is located at the centre of the elongated dust shell. There are small ‘patch-like’ scale structures inner region the shell within 2–3 arcsec from the central star.

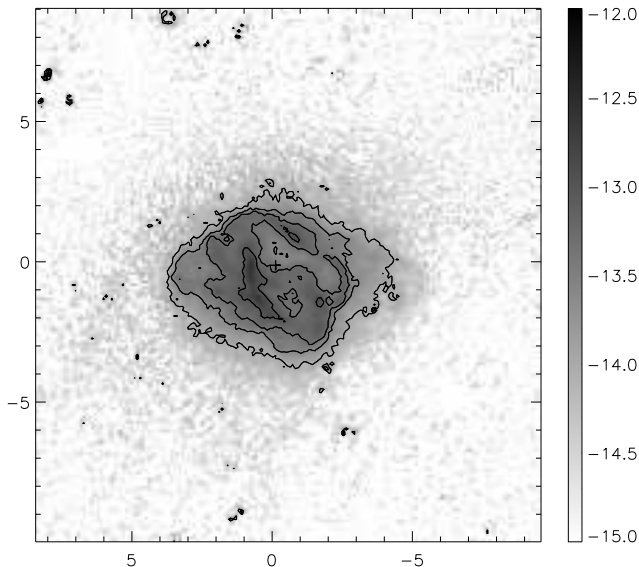


Figure 6. The central region of $H\beta$ (I_ν) image Contour show $\log(I_\nu) = -14, -13.6, -13.3, -13$.

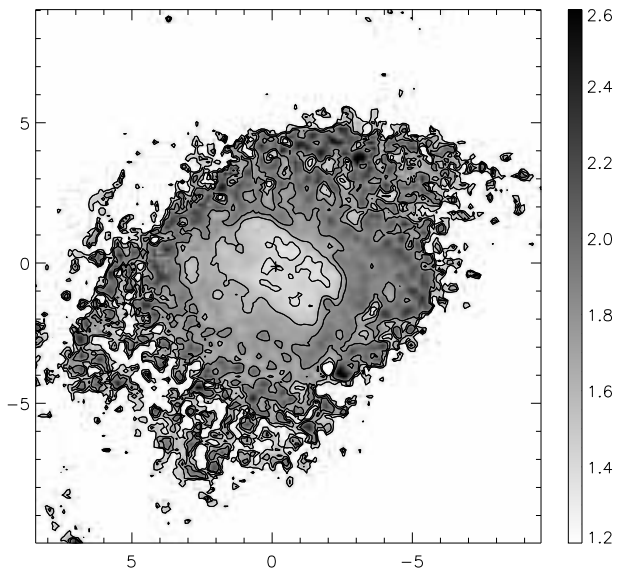


Figure 7. The extinction map. The contour lines show 1.4, 1.6, and 1.8 mag in $E(H\beta - H\alpha)$, and smoothed to $0.14 \text{ arcsec pixel}^{-1}$. The central star is marked as a cross. At the centre, the extinction is 1.4–1.5 mag, while the extinction is higher than 2 mag at $\sim 4 \text{ arcsec}$ from the central star. White points inside the extinction map (e.g. RA offset ~ -2 and Dec offset of ~ -4) are caused by cosmic ray hits on the detector, in the $H\beta$ image.

Cuesta et al. (1995) suggested a reduction in extinction at the centre, using their optical spectroscopy across the centre region. We confirm this, and show the extinction peaks in a shell structure.

The average extinction towards NGC 6537 is reported as $E(B - V) = 1.23$ (Pottasch 2000a), $A_V = 3.4$ (Cuesta et al. 1995), or $C = 1.79 - 2.16$ (Ashley and Hyland 1988). These

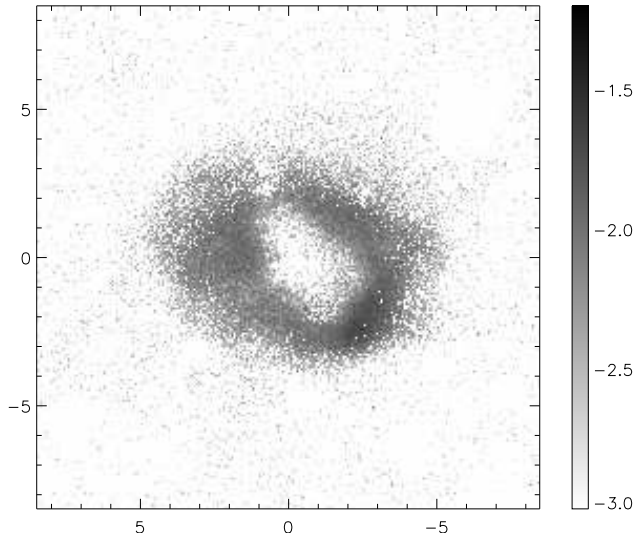


Figure 8. PAH image in Jy arcsec^{-1} .

correspond to $E(H\beta - H\alpha) = 1.50, 1.33, 1.48 - 1.79$, if the interstellar extinction law (Cardelli, Clayton and Mathis 1989) and $A(V)/E(B - V) = 3.1$ are assumed. These values of extinction were derived from hydrogen recombination lines, presumably weighted towards the lines originating from high $H\alpha$ intensity region. In our map, that region has $E(H\beta - H\alpha) = 1.5 \text{ mag}$, which is within previous measurement uncertainties. The average $E(H\beta - H\alpha)$ of the whole region (defined as $E(H\beta - H\alpha)$ higher than 0.2 and smaller than 3.0 mag) is 1.25, and the median is 1.20 mag, which is below $E(H\beta - H\alpha)$ at the high $H\alpha$ region.

3.3 Hierarchy of $H\alpha$, PAHs and extinction

Fig. 8 show the PAH image of the central region. The PAH emission is concentrated in an elongated shell. Comparing with the $H\alpha$ distribution (Fig. 2) shows that the arcs seen in the $H\alpha$ image are also emitting PAHs, but the shapes are not fully coincident: the PAH distribution traces the outer edge of the optical arcs. Slices through the $H\alpha$, PAH and extinction images are plotted in Fig. 9. This shows a radial hierarchy in the shells and rings: the $H\alpha$ rings are found in the innermost region, and PAHs are found at and outside of the $H\alpha$ region, where the extinction is $E(B - V) \sim 1.8 \text{ mag}$, slightly higher than the extinction towards the central star. The extinction increases further outside of the PAH emitting region.

To first approximation, the dense $H\alpha$ emission traces the inner edge of the dust shell, while the PAH emission could be located in a photo-dissociation region. However, confirmation of such a model would require detection and mapping of molecular emission.

4 DISCUSSION

4.1 The central star

The magnitudes of the central star allow us to estimate the luminosity of the central star, and to discuss its evolutionary

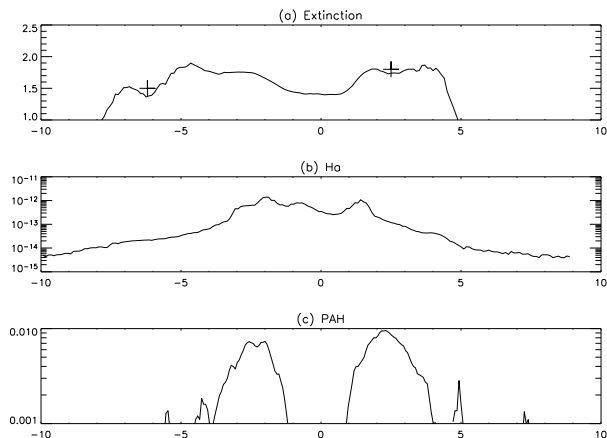


Figure 9. A slice through the extinction map, H α map, and PAH image at constant RA (minus is the south) across the central star. Extinction is smoothed to 0.8 arcsec pixel $^{-1}$ on image. Bumps at Dec offset = -6.2 and 2.5 in the extinction map marked with crosses are artificial (one large spike noise spread to other pixels because of the smoothing).

stage. To derive the luminosity, the effective temperature and extinction towards the centre are needed.

For the extinction towards the central star we take the central extinction measured from H α /H β . This assumes that the ionized region is located within the dust shell. The hierarchy discussed above supports this distribution. We ignore back-scattering which may make the observed extinction slightly higher. If this were important, the dense H α filament located very close to the position of the star could be expected to show lower extinction. However, the filament shows identical extinction to the general inner region.

We estimate the Zanstra temperature using our visual magnitude of the central star and mean extinction, together with the total flux of H β and He 4861 Å (Reay et al. 1984). The Zanstra temperature estimated from helium is 340,000 K. The estimate of Pottasch (2000a) shows a higher Zanstra temperature of 500 000 K. Since we can not estimate the systematic error in our measurements of visual magnitude, this higher temperature could not be ruled out totally at this point.

Given the very high temperature, the various uncertainties on the Zanstra temperatures need to be considered. Some cause the HeII Zanstra temperatures to be too low: high optical depth, internal dust extinction, helium overabundance (Gruenwald and Viegas 2000). A binary companion could make the star appear brighter which would also lead to a lower Zanstra temperature. An excess of stellar photons in the extreme ultraviolet, shortward of the He ionization edge, can cause the Zanstra temperature to be overestimated. Henry and Shipman (1986) discuss the importance of composition: He-poor atmosphere cause the HeII Zanstra temperature to be overestimated, however this effect diminishes at the highest temperatures and is perhaps less likely for a type-I (He-rich) PN. Gabler et al. (1991) mention that shocks within the fast wind can increase the EUV emission and lead to overly high Zanstra temperatures.

From the previous section, the extinction towards the central star is $E(\text{H}\beta - \text{H}\alpha) = 1.40$, which is equivalent with $A(V) = 3.71$. The magnitudes for the four bands where the star is detected, are corrected for this extinction. We fit the resulting fluxes with a black body (Fig. 10) to derive the luminosity of the central star

(L_*) (Table 3). Initially, parameters in Pottasch (2000a) are used; the black body temperature is $T_{\text{bb}} = 500\,000$ K, the distance is $D_0 = 2.4$ kpc, and the stellar radius is $r_0 = 1.16 \times 10^{-2} R_\odot$. With these parameters (case Ia), the fit is within 1σ in the optical but outside of this range at F547M and F631N.

For the next step, we scale the blackbody by a factor a^2 , i.e. the solid angle is $\Omega \approx \pi(r_0/D_0 \times a)^2$. The lowest flux within the uncertainty (1σ) is found at $a = 1.16$ (case Ib) and highest flux is found at $a = 1.38$ (case Ic). The luminosity is calculated with two possibilities for each case, adopting the scaling factor for distance and for radius, respectively. We assume T_{bb} is equivalent with effective temperature T_{eff} . Consequently, the luminosity range is $[7.5\text{--}10.1] \times 10^3 L_\odot$ (Table 3).

Finally, T_{bb} is varied. A lower estimate of the temperature of the central star has been reported, and Casassus et al. (2000) estimated 150 000 K from the ionization levels of the nebula. The fitted result corresponds to case (II) in Table 3. The luminosity is an order of magnitude lower in this case. On the other hand, with our estimated Zanstra temperature of 340 000 K, the luminosity range is $[1.6\text{--}4.6] \times 10^3 L_\odot$ (Table 3). Case IIIa is for the lower limits of the magnitudes errors, and case IIIb is for the upper limits. The black body lines of case III are not plotted in Fig. 10, because the lines overlay with those of case Ib and Ic on this plotting scale.

We plot these estimated L_* and T_{eff} (assuming $T_{\text{bb}} = T_{\text{eff}}$) on the HR diagram with a comparison with the theoretical evolutionary tracks for solar abundances (Blöcker 1995). Fig. 11 shows that the central star is within the highest luminosity as a PN and temperature range if T_{eff} is 500 000 K, whilst if T_{eff} is lower than that, the central star is already in the white dwarf (WD) phase. Different estimates for T_{eff} give totally different luminosities. Nevertheless, the models tend to coincide with the higher mass tracks.

A further constraint on the stellar mass derives from the time scales for the post-AGB evolution (Gesicki and Zijlstra 2000). Higher-mass stars evolve much more rapidly to higher temperature. All models accelerate when evolving through the knee of the HR diagram, and evolution slows dramatically around $10^3 L_\odot$ for the highest mass tracks, and around $300 L_\odot$ for the $3 M_\odot$ track. Indicative post-AGB ages for different tracks are shown in Fig. 11.

Cuesta et al. (1995) reported that the central region of NGC 6537 has an expansion velocity of 18 km s^{-1} . Corradi and Schwarz (1993) also found a similar velocity. In previous discussion, we obtained distance of 0.9-2.4 kpc. If we assume the distance of 1.5 kpc, the dynamical age of the dust shell should be about 1600 years, assuming that the shell has been constantly expanding with this speed and that the current radius is 4 arcsec. Models with core masses in the range $0.696 - 0.943 M_\odot$ gives a possible fit for a luminosity in the range $2.5 < \log L < 3$. Lower-mass tracks evolve too slowly before reaching the dashed region. The best fit track has a core mass of $\approx 0.7 - 0.9 M_\odot$ and progenitor mass of $3\text{--}7 M_\odot$.

The comparison of ages and stellar parameters favours a lower temperature for the central star of NGC 6537, in the region $1.5\text{--}2.5 \times 10^5$ K. This is below the HeII Zanstra temperature, suggesting the latter may have been overestimated.

The progenitor mass heavily depends on the mass lost during the AGB phase, and is less well constrained than the core mass. The relation between final and initial mass may differ from the ones of the Blöcker tracks. However, the derived core mass is high for PNe (Gesicki and Zijlstra 2000) and is consistent with a higher-mass progenitor. The nitrogen and helium enrichment of this type-I PN (Peimbert 1978) also suggests a high-mass progenitor (c.f. Pottasch et al. 2000b).

The bipolar lobes have velocities of $\sim 350 \text{ km s}^{-1}$. This gives a similar expansion age to that of the core. This suggest the bipo-

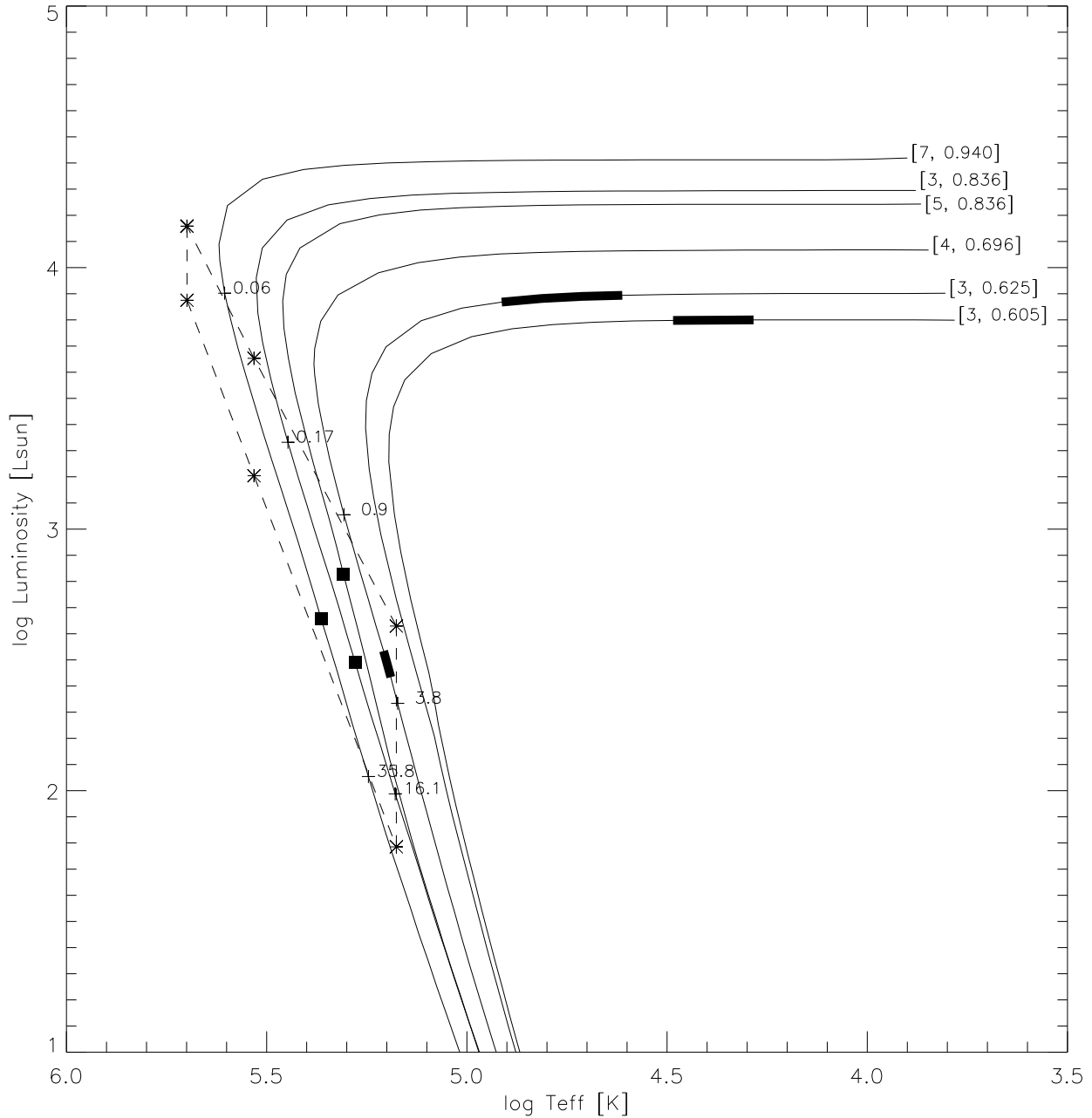


Figure 11. The estimated luminosity and T_{eff} of the central star of NGC 6537, plotted on the evolutionary tracks of post-AGB stars Blöcker (1995). The dashed line encloses the estimated temperature and luminosity range (the asterisks show the fit calculations). The numbers in the parenthesis are M_{ZAMS} and the core mass at the tip of the AGB, in solar units, for Blöcker (1995)’s models. The numbers on the plus signs show the age in 10^3 years after the AGB phase. The bold lines on the evolutionary tracks indicate the age of 1000–2000 years after the AGB phase, suggested by the dynamical age. This age range is estimated from the size of the dust shell. $M_c \approx 0.7 - 0.9 M_{\odot}$ and M_{ZAMS} of $3-7 M_{\odot}$ is likely for NGC 6537.

lar structure and the dust shell formed near-simultaneously, and were present very soon after the onset of the post-AGB evolution.

4.2 Dust within NGC 6537

The temperature of the circumstellar dust shell decreases as the circumstellar shell expands and the central star evolves from AGB star to post-AGB star and PN (van der Veen and Habing 1988).

The cool far-infrared excess found in PNe is the remnant of the large mass loss phase at the end of AGB phase.

The temperature of the dust shell is estimated from the central star parameters and the distance, discussed in the previous section. The high extinction is mainly found within 2–4 arcsec from the star. Ignoring the projection effects, an inner radius of 2 arcsec and outer radius of 4 arcsec are assumed. We can estimate the dust temperature T_d from $d_d/R_{\star} = (T_{\text{eff}}/T_d)^2$, if the

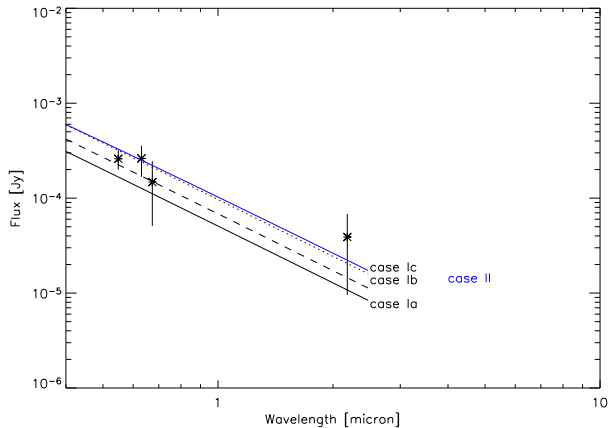


Figure 10. The extinction-corrected flux of the central star, and the black body fits. The parameters are listed in Table 3. Case Ic and case II have almost the same line, the dashed line is for case Ic, and the blue line is for case II.

Table 3. Fitting results to the fluxes.

	T_{bb} [K]	a	L_* [L_{\odot}]
case Ia	500 000	1.00	7.5×10^3
case Ib	500 000	1.16	$[7.5-10.1] \times 10^3$
case Ic	500 000	1.38	$[7.5-14.4] \times 10^3$
case II	150 000	2.64	61–426
case IIIa	340 000	1.41	$[1.6-3.2] \times 10^3$
case IIIa	340 000	1.68	$[1.6-4.6] \times 10^3$

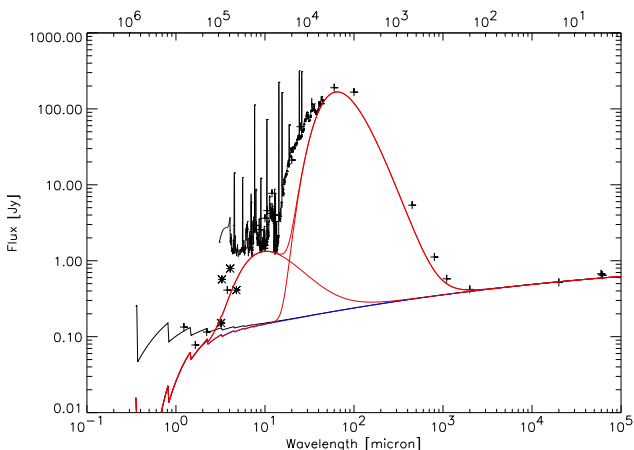


Figure 12. The measured infrared to radio flux of the core of NGC 6537. The data are from our ISAAC observations at L and M-bands, ISO/SWS, IRAS, Whitelock (1985), Phillips and Cuesta (1994), Cohen and Barlow (1980), and Hoare et al. (1992). The solid line is a total of calculated free-free and bound-free emission, scaled to the radio data. Two black body curves are shown (dashed lines) to emphasize the dust excess on top of the extinction corrected free-free and bound-free continuum.

dust grains are directly heated by the central star, where d_d is the distance of a dust particle from the central star and R_* is the stellar radius. For $T_{\text{eff}}=3.4 \times 10^5$ K, scale $a = 2.6$ (Case IIIa in Table 3), T_d is 45 K and 32 K at 2 arcsec, and 4 arcsec in radius, respectively. This can be compared to the dust condensation (and formation) temperature, about 1 000 K for silicate. The dust grains formed much closer to the star, during the AGB, and the grains have moved outwards.

Infrared spectra (Fig. 12) show two peaks in the dust excess. The colder shell has a peak at about 50–60 μm , which corresponds to temperature of about 50 K. This is consistent with the above estimated temperature from the dust radius. The hotter dust peaks around 10 μm , with a temperature around 300 K. This hotter dust cannot be located much closer to the star, as the optical and infrared images indicate a central cavity. Instead this emission must arise for a component which reaches higher temperatures, either because it consists of smaller grains, or receiving additional heating. This component has a much smaller mass than the cold dust.

The extinction allows us to map the cold dust at much higher resolution than would otherwise be possible. Imaging thermal emission of cold dust requires far-infrared space telescopes such as ISO and Spitzer; their small apertures are “resolution-challenged” (Rieke et al. 2004); e.g. the 6-arcsec resolution at 24 μm for Spitzer would leave the core of NGC 6537 unresolved. In contrast, our extinction map has a resolution of 0.14 arcsec per pixel. As the dust shell closest to the core was ejected last, this gives a unique handle on the morphology of the final AGB wind, and helps constrain the origin of the bipolar morphology.

The extinction map is far more symmetric than either the HST or the infrared images. The structure delineated by the inner cavity shows an elongation approximately (but not perfectly) along the bipolar axis, with an axial ratio of 1.5:1. For comparison, the optical image shows an elongation of the full structure (at the faintest emission levels) of approximately 4:1. A large amplification has clearly taken place. The structure shows that the mass loss on the AGB was much more spherically symmetric than the current PN would suggest.

The shell is relatively thick, with an outer radius at least twice the inner radius. The optical emission appears embedded in the dust shell, and so the extinction map measures the extinction from the front shell only (this is the reason we can apply the extinction map for the central star). The observed ratio of peak extinction over central extinction (in mag) of 1.4, would require an outer radius of the dust shell of 6 arcsec, for an observed inner radius of 3 arcsec and uniform density. However, the extinction includes an ISM foreground component, and the observed extinction ratio is therefore a lower limit. A higher ratio corresponds to a smaller outer radius.

The dust shell may well extend further out than derived from the extinction map: the optical $H\beta$ flux becomes too faint to accurately determine extinction values. But the estimate above makes is likely that the dense part of the shell does not extend much beyond the limits of the map. The AGB wind will extend much further as a $1/r^2$ envelope, as suggested by the large extent of the optical emission. But an extended $1/r^2$ envelope would not give rise to a large difference in extinction over the (small) central hole. We conclude that inner dust shell is distinct from the outer AGB wind, either tracing a short lived ($< 10^4$ yr) event of very high mass loss, and/or swept-up gas.

The final point to note is that we can exclude the ‘thin’ almost-edge-on disk which was proposed by Cuesta et al. (1995). This would give rise to a narrow, extinction structure, with a strongly elongated ‘higher extinction region’ perpendicular to the polar axis. The observed structure is only mildly elongated, and the direction of elongation is opposite to what would be expected from a thin disk. The observed elongation is reminiscent of a cylindrical structure, or of a torus with thickness comparable to

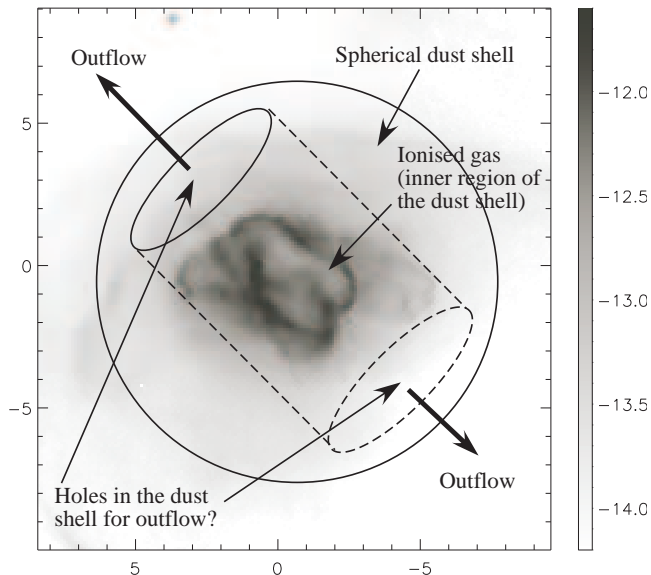


Figure 13. Schematic view of shell. Circumstellar shell may be elongated along the holes so as it looks like a ‘torus’.

its radius (Fig. 13), but apart from the polar holes the structure show no clear deviation from spherical symmetry.

An inevitable question is whether this dust shell is responsible for collimating the bipolar flow. In favour of this is the location, at the neck of the flow, and the compact size, 10 per cent of that of the lobes. The similarity of dynamical age between the dust shell and the shell shows that the collimation first occurred very early in the evolution, during the AGB or in the early post-AGB wind. This may argue against versions of the Interacting Stellar Winds where the shaping is due to the fast wind from the central star of the PN, as this wind only develops in the later post-AGB evolution, at higher stellar temperature.

The timing of the lobes is consistent with current ideas that the shaping originally occurs due to a change in the wind morphology at the end of the high mass-loss phase (Zijlstra et al. 2001). A model which could fit the observed characteristics (a symmetric shell with lower densities only towards the poles) is presented by Sahai and Trauger (1998): they propose that a fast jet-like wind punches holes in the spherical AGB shell, and that the subsequent post-AGB evolution amplifies this sudden departure from spherical shape.

Such a model may require a binary companion as source for the jet. There is no evidence either against or in favour of a binary at the core of NGC 6537. The optical magnitude rules out a solar-like star, but a fainter red dwarf or a white dwarf are not excluded. The near infrared detection may show some excess emission, but this cannot be taken as evidence for a red companion. For comparison, the central star of the very similar PN NGC 6302 has been shown to have an infrared excess which is not a stellar continuum (Matsuura et al. 2005).

4.3 Hierarchical structure

In NGC 6537, a hierarchical structure is found, with the peak of PAH intensity located further out than that of $H\alpha$. This is consistent with observations in other objects (NGC 7027 (Woodward et al. 1989) and NGC 6302 (Matsuura et al. 2005)), where PAH emission is located outside of the ionised gas. The extinction continues to increase outside the PAH region, and PAH emission is not found where the extinction is high (~ 5 arcsec). This can be a consequence of the lack of photo excita-

tion in the high extinction region, or a difference in abundances (Matsuura et al. 2004).

The abundance analysis from optical line ratios shows that NGC 6537 is oxygen-rich (Pottasch et al. 2000b). The presence of PAHs (Roche and Aitken 1986), which are normally assumed to be formed from carbon-rich gas, is unexpected but this chemical dichotomy is also seen in a few other PNe (Matsuura et al. 2005). PAHs have smaller absorption coefficients in the optical than silicate grains, and PAHs are unlikely to be the source of high extinction in the optical: amorphous silicate is likely the main contributor to the optical extinction. Crystalline silicates have also been detected in NGC 6537 (Molster et al. 2002). As the peak of extinction occurs outside of the PAH emission peak, the silicate grains are located outside the location of the PAHs. This can indicate that the silicates pre-date the PAHs.

Hydrogen molecules are detected in NGC 6537: the brightest H_2 region is found around the ionized core, corresponding to the high extinction shell (Davis et al. 2003). The presence of H_2 shows that the dust shell is partly molecular, and the separation between extinction and $H\alpha$ traces an ionization front. The PAH emission is located close to the ionization front but the precise relation, and whether the PAHs formed in-situ or also date from the AGB, remains to be determined.

The hierarchy, with the PAH located in between the ionized and molecular gas, suggests that the PAH emission may be associated with the photo-dissociation region of the molecular dust shell. Following (Matsuura et al. 2004), we associate the hot dust component (Section 4.2) with dust located in the PAH-emitting region.

5 CONCLUSION

The high-resolution images presented in this paper detect the central star of NGC 6537. The agreement between the optical and infrared images secure the identification. The magnitudes are relatively uncertain, due to the high background, but the derived values agree within the uncertainties with a hot black body. The luminosity depends on the assumed temperature: dynamical considerations, comparing with the stellar evolution tracks, argues for relatively low luminosities $\sim 10^3 L_\odot$. This gives a temperature in the range $1.5\text{--}2.5 \times 10^5$ K, slightly lower than the HeII Zanstra temperature of 3.4×10^5 K. We derive a core mass around $M_c \approx 0.7\text{--}0.9 M_\odot$, and a progenitor mass $M_i = 3\text{--}7 M_\odot$.

The progenitor mass is consistent with the classification of NGC 6537 as a type-I PN. Bipolar PNe have been suggested to have higher than average initial mass: our results do not conflict with this.

The extinction map is not uniform inside NGC 6537, but shows a shell structure of inner radius of 2 arcsec and outer radius of at least 4 arcsec. The central star is located at the centre of the near-symmetric extinction distribution. The dust shell traces the high mass-loss phase during the AGB phase, and was expelled from the central star about 1400 years ago. There is no evidence for a thin disk, as has been suggested. The dust shell is far more compact, and far more symmetric than the extended bipolar lobes. A thick torus or cylindrical structure can fit the observed extinction map.

The dynamical age of the lobes and dust shell are very similar. This suggests that the origin of the bipolarity should be close to the end of the AGB. The largely symmetric dust shell, combined with the strongly bipolar lobes, are consistent with models of a fast change of wind structure at the end of the AGB mass loss.

The structure shows radial hierarchy, with the ionized core located at the inner edge of the dust shell, and the PAH emission in between, tentatively associated with the photo-dissociation region.

6 ACKNOWLEDGEMENTS

We are grateful for the support by the ESO staff during observations. The ESO/ST-ECF Science Archive was used for this study. M.M. is financially supported by PPARC.

REFERENCES

- Ashley, M.C.B., Hyland, A.R., 1988, *ApJ* 331, 532
 Balick B., Frank A., 2002, *ARA&A*, 40, 439
 Blöcker, T., 1995, *A&A* 299, 755
 Cardelli, J.A., Clayton, G.C., & Mathis, J.S., 1989, *ApJ* 345, 245
 Casassus, S., Roche, P.F., & Barlow, M.J., 2000, *MNRAS* 314, 657
 Cohen, M., Barlow, M.J., 1980, *ApJ* 238, 585
 Corradi, R.L.M., Schwarz, H.E., 1993, *A&A* 269, 462
 Cuesta, L., Phillips, J.P., Mampaso, A., 1995, *A&A* 304, 475
 Davis C.J., Smith, M.D., Stern, L., Kerr, Th.H., Chiar, J.E., 2003, *MNRAS* 344, 262
 Gabler, R., Kudritzki, R. P., Mendez, R. H., 1991, *A&A*, 245, 587
 Gathier, R., Pottasch, S.R., 1988, *A&A* 197, 266
 Gesicki, K., Zijlstra A.A., 2000, *A&A*, 358, 1058
 Gruenwald, R., Viegas, S. M., 2000, *ApJ*, 543, 889
 Habing, H.J., 1996, *A&ARv* 7, 97
 Henry, R.B.C., Shipman, H.L., 1986, *ApJ*, 311, 774
 Hoare, M.G., Roche, P.F., & Clegg, R.E.S., 1992, *MNRAS* 258, 257
 Icke V. 2003, *A&A* 405, L11
 Izumiura, H., Hashimoto, O., Kawara, K., Yamamura, I., Waters, L.B.F.M., 1996, *A&A* 315, L221
 Kaler, J.B., Jacoby, G.H., 1989, *ApJ* 345, 871
 Kastner, J.H., Weintraub, D.A., Gatley, I., Merrill, K.M., Probst, R.G., 1996, *ApJ* 462, 777
 Kwok, S., 1982, *ApJ*, 258, 280
 Matsuura, M., Zijlstra, A.A., Molster, F.J., et al., 2004, *ApJ*, 604, 791
 Matsuura, M., Zijlstra, A.A., Molster F.J., Waters, L.B.F.M., Nomura, H., Sahai R., Hoare, M.G., 2005, *MNRAS*, 359, 383
 Molster, F.J., Waters, L.B.F.M., & Tielens, A.G.G.M., 2002, *A&A* 382, 222
 Olofsson, H., Bergman, P., Lucas, R., Eriksson, K., Gustafsson, B., Biegging, J.H., 2000, *A&A* 353, 583
 Peimbert, M., 1978, *IAU Symposium 76, Planetary Nebulae*, ed. Y. Terzian (Dordrecht), p215
 Phillips, J.P., Cuesta, L., 1994, *A&AS* 104, 169
 Pottasch, S.R., 2000a, *A&A* 362, L17
 Pottasch, S.R., Beintema, D.A., Feibelman, W.A., 2000b, *A&A* 363, 767
 Reay, N.K., Pottasch, S.R., Atherton, P.D., Taylor, K., 1984 *A&A* 137, 113
 Rieke, G.H., Young, E.T., Engelbracht, C.W., Kelly, D.M., Low, F.J., et al., 2004, *ApJS*, 154, 25
 Roche, P. F., & Aitken, D. K., 1986, *MNRAS* 221, 63
 Sahai, R., Trauger, J.T., 1998, *AJ*, 116, 1357
 Storey, P.J., Hummer, D.G., 1995, *MNRAS* 272, 41
 van der Veen, W.E.C.J., Habing, H.J., 1988, *A&A* 194, 125
 Whitelock, P., 1985, *MNRAS* 213, 59
 Woodward, C.E., Pipher, J.L., Shure, M., Forrest, W.J., Sellgren, K., 1989, *ApJ* 342, 860
 Zijlstra, A.A., Chapman, J.M., te Lintel Hekkert, P., et al., 2001, *MNRAS*, 322, 280